

Search for radiative leptonic decay $D^+ \rightarrow \gamma e^+ \nu_e$ using deep learning*

M. Ablikim (麦迪娜)¹ M. N. Achasov^{4,c} P. Adlarson⁷⁶ X. C. Ai (艾小聪)⁸¹ R. Aliberti³⁵ A. Amoroso^{75A,75C}
 Q. An (安琪)^{72,58,a} Y. Bai (白羽)⁵⁷ O. Bakina³⁶ Y. Ban (班勇)^{46,h} H.-R. Bao (包浩然)⁶⁴ V. Batzskaya^{1,44}
 K. Begzsuren³² N. Berger³⁵ M. Berlowski⁴⁴ M. Bertani^{28A} D. Bettoni^{29A} F. Bianchi^{75A,75C} E. Bianco^{75A,75C}
 A. Bortone^{75A,75C} I. Boyko³⁶ R. A. Briere⁵ A. Brueggemann⁶⁹ H. Cai (蔡浩)⁷⁷ M. H. Cai (蔡铭航)^{38,k,l}
 X. Cai (蔡啸)^{1,58} A. Calcaterra^{28A} G. F. Cao (曹国富)^{1,64} N. Cao (曹宁)^{1,64} S. A. Cetin^{62A} X. Y. Chai (柴新宇)^{46,h}
 J. F. Chang (常劲帆)^{1,58} G. R. Che (车国荣)⁴³ Y. Z. Che (车逾之)^{1,58,64} G. Chelkov^{36,b} C. Chen (陈琛)⁴³
 C. H. Chen (陈春卉)⁹ Chao Chen (陈超)⁵⁵ G. Chen (陈刚)¹ H. S. Chen (陈和生)^{1,64} H. Y. Chen (陈弘扬)²⁰
 M. L. Chen (陈玛丽)^{1,58,64} S. J. Chen (陈申见)⁴² S. L. Chen (陈思璐)⁴⁵ S. M. Chen (陈少敏)⁶¹ T. Chen (陈通)^{1,64}
 X. R. Chen (陈旭荣)^{31,64} X. T. Chen (陈肖婷)^{1,64} X. Y. Chen (陈心宇)^{12,g} Y. B. Chen (陈元柏)^{1,58} Y. Q. Chen³⁴
 Z. J. Chen (陈卓俊)^{25,i} Z. K. Chen (陈梓康)⁵⁹ S. K. Choi¹⁰ X. Chu (初晓)^{12,g} G. Cibirnetto^{29A} F. Cossio^{75C}
 J. J. Cui (崔佳佳)⁵⁰ H. L. Dai (代洪亮)^{1,58} J. P. Dai (代建平)⁷⁹ A. Dbeyssi¹⁸ R. E. de Boer³ D. Dedovich³⁶
 C. Q. Deng (邓创旗)⁷³ Z. Y. Deng (邓子艳)¹ A. Denig³⁵ I. Denysenko³⁶ M. Destefanis^{75A,75C} F. De Mori^{75A,75C}
 B. Ding (丁彪)^{67,1} X. X. Ding (丁晓萱)^{46,h} Y. Ding (丁逸)³⁴ Y. Ding (丁勇)⁴⁰ Y. X. Ding (丁玉鑫)³⁰
 J. Dong (董静)^{1,58} L. Y. Dong (董燎原)^{1,64} M. Y. Dong (董明义)^{1,58,64} X. Dong (董翔)⁷⁷ M. C. Du (杜蒙川)¹
 S. X. Du (杜少旭)^{12,g} S. X. Du (杜书先)⁸¹ Y. Y. Duan (段尧予)⁵⁵ Z. H. Duan (段宗欢)⁴² P. Egorov^{36,b}
 G. F. Fan (樊高峰)⁴² J. J. Fan (樊俊杰)¹⁹ Y. H. Fan (范宇晗)⁴⁵ J. Fang (方进)⁵⁹ J. Fang (方建)^{1,58}
 S. S. Fang (房双世)^{1,64} W. X. Fang (方文兴)¹ Y. Q. Fang (方亚泉)^{1,58} R. Farinelli^{29A} L. Fava^{75B,75C} F. Feldbauer³
 G. Felici^{28A} C. Q. Feng (封常青)^{72,58} Y. T. Feng (冯珂潼)^{72,58} M. Fritsch³ C. D. Fu (傅成栋)¹ J. L. Fu (傅金林)⁶⁴
 Y. W. Fu (傅亦威)^{1,64} H. Gao (高涵)⁶⁴ X. B. Gao (高鑫博)⁴¹ Y. Gao (高扬)^{72,58} Y. N. Gao (高原宁)^{46,h}
 Y. N. Gao (高语浓)¹⁹ Y. Y. Gao (高洋洋)³⁰ S. Garbolino^{75C} I. Garzia^{29A,29B} P. T. Ge (葛潘婷)¹⁹
 Z. W. Ge (葛振武)⁴² C. Geng (耿聪)⁵⁹ E. M. Gersabeck⁶⁸ A. Gilman⁷⁰ K. Goetzen¹³ J. D. Gong (龚家鼎)³⁴
 L. Gong (龚丽)⁴⁰ W. X. Gong (龚文煊)^{1,58} W. Gradl³⁵ S. Gramigna^{29A,29B} M. Greco^{75A,75C} M. H. Gu (顾旻皓)^{1,58}
 Y. T. Gu (顾运厅)¹⁵ C. Y. Guan (关春懿)^{1,64} A. Q. Guo (郭爱强)³¹ L. B. Guo (郭立波)⁴¹ M. J. Guo (国梦娇)⁵⁰
 R. P. Guo (郭如盼)⁴⁹ Y. P. Guo (郭玉萍)^{12,g} A. Guskov^{36,b} J. Gutierrez²⁷ K. L. Han (韩坤霖)⁶⁴ T. T. Han (韩婷婷)¹
 F. Hanisch³ K. D. Hao (郝科迪)^{72,58} X. Q. Hao (郝喜庆)¹⁹ F. A. Harris⁶⁶ K. K. He (何凯凯)⁵⁵
 K. L. He (何康林)^{1,64} F. H. Heinsius³ C. H. Heinz³⁵ Y. K. Heng (衡月昆)^{1,58,64} C. Herold⁶⁰ T. Holtmann³
 P. C. Hong (洪鹏程)³⁴ G. Y. Hou (侯国一)^{1,64} X. T. Hou (侯贤涛)^{1,64} Y. R. Hou (侯颖锐)⁶⁴ Z. L. Hou (侯治龙)¹
 H. M. Hu (胡海明)^{1,64} J. F. Hu (胡继峰)^{56,j} Q. P. Hu (胡启鹏)^{72,58} S. L. Hu (胡圣亮)^{12,g} T. Hu (胡涛)^{1,58,64}
 Y. Hu (胡誉)¹ Z. M. Hu (胡忠敏)⁵⁹ G. S. Huang (黄光顺)^{72,58} K. X. Huang (黄凯旋)⁵⁹ L. Q. Huang (黄麟钦)^{31,64}
 P. Huang (黄盼)⁴² X. T. Huang (黄性涛)⁵⁰ Y. P. Huang (黄燕萍)¹ Y. S. Huang (黄永盛)⁵⁹ T. Hussain⁷⁴
 N. Hüsen³⁵ N. in der Wiesche⁶⁹ J. Jackson²⁷ Q. Ji (纪全)¹ Q. P. Ji (姬清平)¹⁹ W. Ji (季旺)^{1,64}

Received 20 March 2025; Accepted 17 April 2025; Published online 18 April 2025

* This work is supported in part by National Key R&D Program of China (2020YFA0406400, 2023YFA1606000, 2020YFA0406300); National Natural Science Foundation of China (NSFC) (11635010, 11735014, 11935015, 11935016, 11935018, 12025502, 12035009, 12035013, 12061131003, 12192260, 12192261, 12192262, 12192263, 12192264, 12192265, 12221005, 12225509, 12235017, 12361141819); the Chinese Academy of Sciences (CAS) Large-Scale Scientific Facility Program; the CAS Center for Excellence in Particle Physics (CCEPP); Joint Large-Scale Scientific Facility Funds of the NSFC and CAS (U1832207); CAS (YSBR-101); 100 Talents Program of CAS; CAS Project for Young Scientists in Basic Research (YSBR-117); The Institute of Nuclear and Particle Physics (INPAC) and Shanghai Key Laboratory for Particle Physics and Cosmology; Agencia Nacional de Investigación y Desarrollo de Chile (ANID), Chile (ANID PIA/APOYO AFB230003); German Research Foundation DFG (FOR5327); Istituto Nazionale di Fisica Nucleare, Italy; Knut and Alice Wallenberg Foundation (2021.0174, 2021.0299); Ministry of Development of Turkey (DPT2006K-120470); National Research Foundation of Korea (NRF-2022R1A2C1092335); National Science and Technology fund of Mongolia; National Science Research and Innovation Fund (NSRF) via the Program Management Unit for Human Resources & Institutional Development, Research and Innovation of Thailand (B50G670107); Polish National Science Centre (2019/35/O/ST2/02907); Swedish Research Council (2019.04595); The Swedish Foundation for International Cooperation in Research and Higher Education (CH2018-7756); U. S. Department of Energy (DE-FG02-05ER41374)



Content from this work may be used under the terms of the Creative Commons Attribution 3.0 licence. Any further distribution of this work must maintain attribution to the author(s) and the title of the work, journal citation and DOI. Article funded by SCOAP³ and published under licence by Chinese Physical Society and the Institute of High Energy Physics of the Chinese Academy of Sciences and the Institute of Modern Physics of the Chinese Academy of Sciences and IOP Publishing Ltd

- X. B. Ji (季晓斌)^{1,64} X. L. Ji (季筱璐)^{1,58} Y. Y. Ji (吉钰瑶)⁵⁰ Z. K. Jia (贾泽坤)^{72,58} D. Jiang (姜地)^{1,64}
H. B. Jiang (姜候兵)⁷⁷ P. C. Jiang (蒋沛成)^{46,h} S. J. Jiang (蒋思婧)⁹ T. J. Jiang (蒋庭俊)¹⁶ X. S. Jiang (江晓山)^{1,58,64}
Y. Jiang (蒋艺)⁶⁴ J. B. Jiao (焦健斌)⁵⁰ J. K. Jiao (焦俊坤)³⁴ Z. Jiao (焦铮)²³ S. Jin (金山)⁴² Y. Jin (金毅)⁶⁷
M. Q. Jing (荆茂强)^{1,64} X. M. Jing (景新媚)⁶⁴ T. Johansson⁷⁶ S. Kabana³³ N. Kalantar-Nayestanaki⁶⁵
X. L. Kang (康晓琳)⁹ X. S. Kang (康晓坤)⁴⁰ M. Kavatsyuk⁶⁵ B. C. Ke (柯百谦)⁸¹ V. Khachatryan²⁷ A. Khoukaz⁶⁹
R. Kiuchi¹ O. B. Kolcu^{62A} B. Kopf³ M. Kuessner³ X. Kui (奎贤)^{1,64} N. Kumar²⁶ A. Kupsc^{44,76} W. Kühn³⁷
Q. Lan (兰强)⁷³ W. N. Lan (兰文宁)¹⁹ T. T. Lei (雷天天)^{72,58} M. Lellmann³⁵ T. Lenz³⁵ C. Li (李聪)⁴³
C. Li (李澄)^{72,58} C. Li (李翠)⁴⁷ C. H. Li (李春花)³⁹ C. K. Li (李春凯)²⁰ D. M. Li (李德民)⁸¹ F. Li (李飞)^{1,58}
G. Li (李刚)¹ H. B. Li (李海波)^{1,64} H. J. Li (李惠静)¹⁹ H. N. Li (李衡讷)^{56,j} Hui Li (李慧)⁴³ J. R. Li (李嘉荣)⁶¹
J. S. Li (李静舒)⁵⁹ K. Li (李科)¹ K. L. Li (李凯璐)^{38,k,l} K. L. Li (李凯璐)¹⁹ L. J. Li (李林健)^{1,64} Lei Li (李蕾)⁴⁸
M. H. Li (李明浩)⁴³ M. R. Li (李明润)^{1,64} P. L. Li (李佩莲)⁶⁴ P. R. Li (李培荣)^{38,k,l} Q. M. Li (李启铭)^{1,64}
Q. X. Li (李起鑫)⁵⁰ R. Li (李燃)^{17,31} S. X. Li (李素娴)¹² T. Li (李腾)⁵⁰ T. Y. Li (李天佑)⁴³ W. D. Li (李卫东)^{1,64}
W. G. Li (李卫国)^{1,a} X. Li (李旭)^{1,64} X. H. Li (李旭红)^{72,58} X. L. Li (李晓玲)⁵⁰ X. Y. Li (李晓宇)^{1,8}
X. Z. Li (李绪泽)⁵⁹ Y. Li (李洋)¹⁹ Y. G. Li (李彦谷)^{46,h} Y. P. Li (李雁鹏)³⁴ Z. J. Li (李志军)⁵⁹ Z. Y. Li (李紫阳)⁷⁹
C. Liang (梁畅)⁴² H. Liang (梁昊)^{72,58} Y. F. Liang (梁勇飞)⁵⁴ Y. T. Liang (梁羽铁)^{31,64} G. R. Liao (廖广睿)¹⁴
L. B. Liao (廖立波)⁵⁹ M. H. Liao (廖明华)⁵⁹ Y. P. Liao (廖一朴)^{1,64} J. Libby²⁶ A. Limphirat⁶⁰ C. C. Lin (蔺长城)⁵⁵
C. X. Lin (林创新)⁶⁴ D. X. Lin (林德旭)^{31,64} L. Q. Lin (邵麟笙)³⁹ T. Lin (林韬)¹ B. J. Liu (刘北江)¹
B. X. Liu (刘宝鑫)⁷⁷ C. Liu (刘成)³⁴ C. X. Liu (刘春秀)¹ F. Liu (刘芳)¹ F. H. Liu (刘福虎)⁵³ Feng Liu (刘峰)⁶
G. M. Liu (刘国明)^{56,j} H. Liu (刘昊)^{38,k,l} H. B. Liu (刘宏邦)¹⁵ H. H. Liu (刘欢欢)¹ H. M. Liu (刘怀民)^{1,64}
Huihui Liu (刘汇慧)²¹ J. B. Liu (刘建北)^{72,58} J. J. Liu (刘佳佳)²⁰ K. Liu (刘凯)^{38,k,l} K. Liu (刘坤)⁷³
K. Y. Liu (刘魁勇)⁴⁰ Ke Liu (刘珂)²² L. Liu (刘亮)^{72,58} L. C. Liu (刘良辰)⁴³ Lu Liu (刘露)⁴³ M. H. Liu (刘美宏)^{12,g}
P. L. Liu (刘佩莲)¹ Q. Liu (刘倩)⁶⁴ S. B. Liu (刘树彬)^{72,58} T. Liu (刘桐)^{12,g} W. K. Liu (刘维克)⁴³
W. M. Liu (刘卫民)^{72,58} W. T. Liu (刘婉婷)³⁹ X. Liu (刘翔)^{38,k,l} X. Liu (刘鑫)³⁹ X. L. Liu (刘兴淋)^{12,g}
X. Y. Liu (刘雪吟)⁷⁷ Y. Liu (刘英)^{38,k,l} Y. Liu (刘义)⁸¹ Y. Liu (刘媛)⁸¹ Y. B. Liu (刘玉斌)⁴³
Z. A. Liu (刘振安)^{1,58,64} Z. D. Liu (刘宗德)⁹ Z. Q. Liu (刘智青)⁵⁰ X. C. Lou (娄辛丑)^{1,58,64} F. X. Lu (卢飞翔)⁵⁹
H. J. Lu (吕海江)²³ J. G. Lu (吕军光)^{1,58} Y. Lu (卢宇)⁷ Y. H. Lu (卢洪宏)^{1,64} Y. P. Lu (卢云鹏)^{1,58}
Z. H. Lu (卢泽辉)^{1,64} C. L. Luo (罗成林)⁴¹ J. R. Luo (罗家瑞)⁵⁹ J. S. Luo (罗家顺)^{1,64} M. X. Luo (罗民兴)⁸⁰
T. Luo (罗涛)^{12,g} X. L. Luo (罗小兰)^{1,58} Z. Y. Lv (吕在裕)²² X. R. Lyu (吕晓睿)^{64,p} Y. F. Lyu (吕翌丰)⁴³
Y. H. Lyu (吕云鹤)⁸¹ F. C. Ma (马凤才)⁴⁰ H. Ma (马衡)⁷⁹ H. L. Ma (马海龙)¹ J. L. Ma (马俊力)^{1,64}
L. L. Ma (马连良)⁵⁰ L. R. Ma (马立瑞)⁶⁷ Q. M. Ma (马秋梅)¹ R. Q. Ma (马润秋)^{1,64} R. Y. Ma (马若云)¹⁹
T. Ma (马腾)^{72,58} X. T. Ma (马晓天)^{1,64} X. Y. Ma (马骁妍)^{1,58} Y. M. Ma (马玉明)³¹ F. E. Maas¹⁸ I. MacKay⁷⁰
M. Maggiora^{75A,75C} S. Malde⁷⁰ Q. A. Malik⁷⁴ Y. J. Mao (冒亚军)^{46,h} Z. P. Mao (毛泽普)¹ S. Marcello^{75A,75C}
F. M. Melendi^{29A,29B} Y. H. Meng (孟琰皓)⁶⁴ Z. X. Meng (孟召霞)⁶⁷ J. G. Messchendorp^{13,65} G. Mezzadri^{29A}
H. Miao (妙晗)^{1,64} T. J. Min (闵天觉)⁴² R. E. Mitchell²⁷ X. H. Mo (莫晓虎)^{1,58,64} B. Moses²⁷ N. Yu. Muchnoi^{4,c}
J. Muskalla³⁵ Y. Nefedov³⁶ F. Nerling^{18,e} L. S. Nie (聂麟苏)²⁰ I. B. Nikolaev^{4,c} Z. Ning (宁哲)^{1,58} S. Nisar^{11,m}
Q. L. Niu (牛祺乐)^{38,k,l} W. D. Niu (牛文迪)^{12,g} S. L. Olsen^{10,64} Q. Ouyang (欧阳群)^{1,58,64} S. Pacetti^{28B,28C}
X. Pan (潘祥)⁵⁵ Y. Pan (潘越)⁵⁷ A. Pathak¹⁰ Y. P. Pei (裴宇鹏)^{72,58} M. Pelizaeus³ H. P. Peng (彭海平)^{72,58}
Y. Y. Peng (彭云翊)^{38,k,l} K. Peters^{13,e} J. L. Ping (平加伦)⁴¹ R. G. Ping (平荣刚)^{1,64} S. Plura³⁵ F. Z. Qi (齐法制)¹
H. R. Qi (漆红荣)⁶¹ M. Qi (祁鸣)⁴² S. Qian (钱森)^{1,58} W. B. Qian (钱文斌)⁶⁴ C. F. Qiao (乔从丰)⁶⁴
J. H. Qiao (乔佳辉)¹⁹ J. J. Qin (秦佳佳)⁷³ J. L. Qin (覃嘉良)⁵⁵ L. Q. Qin (秦丽清)¹⁴ L. Y. Qin (秦龙宇)^{72,58}
P. B. Qin (秦鹏勃)⁷³ X. P. Qin (覃潇平)^{12,g} X. S. Qin (秦小帅)⁵⁰ Z. H. Qin (秦中华)^{1,58} J. F. Qiu (邱进发)¹
Z. H. Qu (屈子皓)⁷³ C. F. Redmer³⁵ A. Rivetti^{75C} M. Rolo^{75C} G. Rong (荣刚)^{1,64} S. S. Rong (荣少石)^{1,64}
F. Rosini^{28B,28C} Ch. Rosner¹⁸ M. Q. Ruan (阮曼奇)^{1,58} S. N. Ruan (阮氏宁)⁴³ N. Salone⁴⁴ A. Sarantsev^{36,d}
Y. Schelhaas³⁵ K. Schoenning⁷⁶ M. Scodeggio^{29A} K. Y. Shan (尚科羽)^{12,g} W. Shan (单葳)²⁴
X. Y. Shan (单心钰)^{72,58} Z. J. Shang (尚子杰)^{38,k,l} J. F. Shangguan (上官剑锋)¹⁶ L. G. Shao (邵立港)^{1,64}
M. Shao (邵明)^{72,58} C. P. Shen (沈成平)^{12,g} H. F. Shen (沈宏飞)^{1,8} W. H. Shen (沈文涵)⁶⁴ X. Y. Shen (沈肖雁)^{1,64}

B. A. Shi (施伯安)⁶⁴ H. Shi (史华)^{72,58} J. L. Shi (石家磊)^{12,g} J. Y. Shi (石京燕)¹ S. Y. Shi (史书宇)⁷³
X. Shi (史欣)^{1,58} H. L. Song (宋海林)^{72,58} J. J. Song (宋娇娇)¹⁹ T. Z. Song (宋天资)⁵⁹ W. M. Song (宋维民)³⁴
Y. J. Song (宋宇镜)^{12,g} Y. X. Song (宋昀轩)^{46,h,n} S. Sosio^{75A,75C} S. Spataro^{75A,75C} F. Stieler³⁵ S. S. Su (苏闪闪)⁴⁰
Y. J. Su (粟杨捷)⁶⁴ G. B. Sun (孙光豹)⁷⁷ G. X. Sun (孙功星)¹ H. Sun (孙昊)⁶⁴ H. K. Sun (孙浩凯)¹
J. F. Sun (孙俊峰)¹⁹ K. Sun (孙开)⁶¹ L. Sun (孙亮)⁷⁷ S. S. Sun (孙胜森)^{1,64} T. Sun^{51,f} Y. C. Sun (孙雨长)⁷⁷
Y. H. Sun (孙益华)³⁰ Y. J. Sun (孙勇杰)^{72,58} Y. Z. Sun (孙永昭)¹ Z. Q. Sun (孙泽群)^{1,64} Z. T. Sun (孙振田)⁵⁰
C. J. Tang (唐昌建)⁵⁴ G. Y. Tang (唐光毅)¹ J. Tang (唐健)⁵⁹ J. J. Tang (唐嘉骏)^{72,58} L. F. Tang (唐林发)³⁹
Y. A. Tang (唐迎澳)⁷⁷ L. Y. Tao (陶璐燕)⁷³ M. Tat⁷⁰ J. X. Teng (滕佳秀)^{72,58} J. Y. Tian (田济源)^{72,58}
W. H. Tian (田文辉)⁵⁹ Y. Tian (田野)³¹ Z. F. Tian (田喆飞)⁷⁷ I. Uman^{62B} B. Wang (王斌)¹ B. Wang (王博)⁵⁹
Bo Wang (王博)^{72,58} C. Wang (王超)¹⁹ Cong Wang (王聪)²² D. Y. Wang (王大勇)^{46,h} H. J. Wang (王泓鉴)^{38,k,1}
J. J. Wang (王家驹)⁷⁷ K. Wang (王科)^{1,58} L. L. Wang (王亮亮)¹ L. W. Wang (王璐仪)³⁴ M. Wang (王萌)⁵⁰
M. Wang^{72,58} N. Y. Wang (王南洋)⁶⁴ S. Wang (王顺)^{12,g} T. Wang (王婷)^{12,g} T. J. Wang (王腾蛟)⁴³
W. Wang (王维)⁷³ W. Wang (王为)⁵⁹ W. P. Wang (王维平)^{35,58,72,o} X. Wang (王轩)^{46,h} X. F. Wang (王雄飞)^{38,k,1}
X. J. Wang (王希俊)³⁹ X. L. Wang (王小龙)^{12,g} X. N. Wang (王新南)¹ Y. Wang (王亦)⁶¹ Y. D. Wang (王雅迪)⁴⁵
Y. F. Wang (王贻芳)^{1,8,64} Y. H. Wang (王英豪)^{38,k,1} Y. J. Wang (王祎景)^{72,58} Y. L. Wang (王艺龙)¹⁹
Y. N. Wang (王燕宁)⁷⁷ Y. Q. Wang (王雨晴)¹ Yaqian Wang (王亚乾)¹⁷ Yi Wang (王义)⁶¹ Yuan Wang (王源)^{17,31}
Z. Wang (王铮)^{1,58} Z. L. Wang (王治浪)⁷³ Z. L. Wang (王治浪)² Z. Q. Wang (王紫祺)^{12,g} Z. Y. Wang (王至勇)^{1,64}
D. H. Wei (魏代会)¹⁴ H. R. Wei⁴³ F. Weidner⁶⁹ S. P. Wen (文硕频)¹ Y. R. Wen (温亚冉)³⁹ U. Wiedner³
G. Wilkinson⁷⁰ M. Wolke⁷⁶ C. Wu (吴晨)³⁹ J. F. Wu (吴金飞)^{1,8} L. H. Wu (伍灵慧)¹ L. J. Wu (吴连近)^{1,64}
L. J. Wu (吴连近)¹⁹ Lianjie Wu (武廉杰)¹⁹ S. G. Wu (吴韶光)^{1,64} S. M. Wu (吴蜀明)⁶⁴ X. Wu (吴潇)^{12,g}
X. H. Wu (伍雄浩)³⁴ Y. J. Wu (吴英杰)³¹ Z. Wu (吴智)^{1,58} L. Xia (夏磊)^{72,58} X. M. Xian (咸秀梅)³⁹
B. H. Xiang (向本后)^{1,64} D. Xiao (肖栋)^{38,k,1} G. Y. Xiao (肖光延)⁴² H. Xiao (肖浩)⁷³ Y. L. Xiao (肖云龙)^{12,g}
Z. J. Xiao (肖振军)⁴¹ C. Xie (谢陈)⁴² K. J. Xie (谢凯吉)^{1,64} X. H. Xie (谢昕海)^{46,h} Y. Xie (谢勇)⁵⁰
Y. G. Xie (谢宇广)^{1,58} Y. H. Xie (谢跃红)⁶ Z. P. Xie (谢智鹏)^{72,58} T. Y. Xing (邢天宇)^{1,64} C. F. Xu^{1,64}
C. J. Xu (许创杰)⁵⁹ G. F. Xu (许国发)¹ H. Y. Xu (许皓月)^{67,2} H. Y. Xu (许皓月)² M. Xu (徐明)^{72,58}
Q. J. Xu (徐庆君)¹⁶ Q. N. Xu³⁰ T. D. Xu (徐腾达)⁷³ W. Xu (许威)¹ W. L. Xu (徐万伦)⁶⁷ X. P. Xu (徐新平)⁵⁵
Y. Xu (徐月)^{12,g} Y. Xu (徐月)⁴⁰ Y. C. Xu (胥英超)⁷⁸ Z. S. Xu (许昭燊)⁶⁴ F. Yan (严芳)^{12,g} H. Y. Yan (闫浩宇)³⁹
L. Yan (严亮)^{12,g} W. B. Yan (鄢文标)^{72,58} W. C. Yan (闫文成)⁸¹ W. H. Yan (闫文昊)⁶ W. P. Yan (闫文鹏)¹⁹
X. Q. Yan (严薛强)^{1,64} H. J. Yang (杨海军)^{51,f} H. L. Yang (杨昊霖)³⁴ H. X. Yang (杨洪勋)¹ J. H. Yang (杨君辉)⁴²
R. J. Yang (杨润佳)¹⁹ T. Yang (杨涛)¹ Y. Yang (杨莹)^{12,g} Y. F. Yang (杨艳芳)⁴³ Y. H. Yang (杨友华)⁴²
Y. Q. Yang (杨永强)⁹ Y. X. Yang (杨逸翔)^{1,64} Y. Z. Yang (杨颖喆)¹⁹ M. Ye (叶梅)^{1,58} M. H. Ye (叶铭汉)^{8,a}
Z. J. Ye (叶子健)^{56,j} Junhao Yin (殷俊昊)⁴³ Z. Y. You (尤郑昀)⁵⁹ B. X. Yu (俞伯祥)^{1,58,64} C. X. Yu (喻纯旭)⁴³
G. Yu¹³ J. S. Yu (俞洁晟)^{25,i} L. Q. Yu (喻丽雯)^{12,g} M. C. Yu⁴⁰ T. Yu (于涛)⁷³ X. D. Yu (余旭东)^{46,h}
Y. C. Yu (郁烨淳)⁸¹ C. Z. Yuan (苑长征)^{1,64} H. Yuan (袁昊)^{1,64} J. Yuan (袁杰)⁴⁵ J. Yuan (袁菁)³⁴ L. Yuan (袁丽)²
S. C. Yuan (苑思成)^{1,64} X. Q. Yuan (袁晓庆)¹ Y. Yuan (袁野)^{1,64} Z. Y. Yuan (袁朝阳)⁵⁹ C. X. Yue (岳崇兴)³⁹
Ying Yue (岳颖)¹⁹ A. A. Zafar⁷⁴ S. H. Zeng^{63A,63B,63C,63D} X. Zeng (曾鑫)^{12,g} Y. Zeng (曾云)^{25,i}
Y. J. Zeng (曾溢嘉)^{1,64} Y. J. Zeng (曾宇杰)⁵⁹ X. Y. Zhai (翟星晔)³⁴ Y. H. Zhan (詹永华)⁵⁹ A. Q. Zhang (张安庆)^{1,64}
B. L. Zhang (张伯伦)^{1,64} B. X. Zhang (张丙新)¹ D. H. Zhang (张丹昊)⁴³ G. Y. Zhang (张广义)¹⁹
G. Y. Zhang (张耕源)^{1,64} H. Zhang (张豪)^{72,58} H. Zhang (张晗)⁸¹ H. C. Zhang (张航畅)^{1,58,64} H. H. Zhang (张宏浩)⁵⁹
H. Q. Zhang (张华桥)^{1,58,64} H. R. Zhang (张浩然)^{72,58} H. Y. Zhang (章红宇)^{1,58} J. Zhang (张进)⁸¹ J. Zhang (张晋)⁵⁹
J. J. Zhang (张进军)⁵² J. L. Zhang (张杰磊)²⁰ J. Q. Zhang (张敬庆)⁴¹ J. S. Zhang (张家声)^{12,g}
J. W. Zhang (张家文)^{1,58,64} J. X. Zhang (张景旭)^{38,k,1} J. Y. Zhang (张建勇)¹ J. Z. Zhang (张景芝)^{1,64}
Jianyu Zhang (张剑宇)⁶⁴ L. M. Zhang (张黎明)⁶¹ Lei Zhang (张雷)⁴² N. Zhang (张楠)⁸¹ P. Zhang (张鹏)^{1,8}
Q. Zhang (张强)¹⁹ Q. Y. Zhang (张秋岩)³⁴ R. Y. Zhang (张若愚)^{38,k,1} S. H. Zhang (张水涵)^{1,64}
Shulei Zhang (张书磊)^{25,i} X. M. Zhang (张晓梅)¹ X. Y. Zhang⁴⁰ X. Y. Zhang (张学尧)⁵⁰ Y. Zhang (张宇)⁷³
Y. Zhang (张瑶)¹ Y. T. Zhang (张亚腾)⁸¹ Y. H. Zhang (张银鸿)^{1,58} Y. M. Zhang (张悦明)³⁹

Y. P. Zhang (张越鹏)^{72,58} Z. D. Zhang (张正德)¹ Z. H. Zhang (张泽恒)¹ Z. L. Zhang (张兆领)³⁴
 Z. L. Zhang (张志龙)⁵⁵ Z. X. Zhang (张泽祥)¹⁹ Z. Y. Zhang (张振宇)⁷⁷ Z. Y. Zhang (张子羽)⁴³
 Z. Z. Zhang (张子扬)⁴⁵ Zh. Zh. Zhang¹⁹ G. Zhao (赵光)¹ J. Y. Zhao (赵静宜)^{1,64} J. Z. Zhao (赵京周)^{1,58}
 L. Zhao (赵玲)¹ L. Zhao (赵雷)^{72,58} M. G. Zhao (赵明刚)⁴³ N. Zhao (赵宁)⁷⁹ R. P. Zhao (赵若平)⁶⁴
 S. J. Zhao (赵书俊)⁸¹ Y. B. Zhao (赵豫斌)^{1,58} Y. L. Zhao (赵艳琳)⁵⁵ Y. X. Zhao (赵宇翔)^{31,64}
 Z. G. Zhao (赵政国)^{72,58} A. Zhemchugov^{36,b} B. Zheng (郑波)⁷³ B. M. Zheng (郑变敏)³⁴ J. P. Zheng (郑建平)^{1,58}
 W. J. Zheng (郑文静)^{1,64} X. R. Zheng (郑心如)¹⁹ Y. H. Zheng (郑阳恒)^{64,p} B. Zhong (钟彬)⁴¹ C. Zhong (钟翠)¹⁹
 H. Zhou (周航)^{35,50,o} J. Q. Zhou (周嘉奇)³⁴ J. Y. Zhou (周佳莹)³⁴ S. Zhou (周帅)⁶ X. Zhou (周详)⁷⁷
 X. K. Zhou (周晓康)⁶ X. R. Zhou (周小蓉)^{72,58} X. Y. Zhou (周兴玉)³⁹ Y. Z. Zhou (周祎卓)^{12,g} A. N. Zhu (朱傲男)⁶⁴
 J. Zhu (朱江)⁴³ K. Zhu (朱凯)¹ K. J. Zhu (朱科军)^{1,58,64} K. S. Zhu (朱康帅)^{12,g} L. Zhu (朱林)³⁴
 L. X. Zhu (朱琳萱)⁶⁴ S. H. Zhu (朱世海)⁷¹ T. J. Zhu (朱腾蛟)^{12,g} W. D. Zhu (朱稳定)⁴¹ W. D. Zhu (朱稳定)^{12,g}
 W. J. Zhu (朱文静)¹ W. Z. Zhu (朱文卓)¹⁹ Y. C. Zhu (朱莹春)^{72,58} Z. A. Zhu (朱自安)^{1,64} X. Y. Zhuang (庄新宇)⁴³
 J. H. Zou (邹佳恒)¹ J. Zu (祖健)^{72,58}

(BESIII Collaboration)

¹Institute of High Energy Physics, Beijing 100049, China

²Beihang University, Beijing 100191, China

³Bochum Ruhr-University, D-44780 Bochum, Germany

⁴Budker Institute of Nuclear Physics SB RAS (BINP), Novosibirsk 630090, Russia

⁵Carnegie Mellon University, Pittsburgh, Pennsylvania 15213, USA

⁶Central China Normal University, Wuhan 430079, China

⁷Central South University, Changsha 410083, China

⁸China Center of Advanced Science and Technology, Beijing 100190, China

⁹China University of Geosciences, Wuhan 430074, China

¹⁰Chung-Ang University, Seoul, 06974, Republic of Korea

¹¹COMSATS University Islamabad, Lahore Campus, Defence Road, Off Raiwind Road, 54000 Lahore, Pakistan

¹²Fudan University, Shanghai 200433, China

¹³GSI Helmholtzcentre for Heavy Ion Research GmbH, D-64291 Darmstadt, Germany

¹⁴Guangxi Normal University, Guilin 541004, China

¹⁵Guangxi University, Nanning 530004, China

¹⁶Hangzhou Normal University, Hangzhou 310036, China

¹⁷Hebei University, Baoding 071002, China

¹⁸Helmholtz Institute Mainz, Staudinger Weg 18, D-55099 Mainz, Germany

¹⁹Henan Normal University, Xinxiang 453007, China

²⁰Henan University, Kaifeng 475004, China

²¹Henan University of Science and Technology, Luoyang 471003, China

²²Henan University of Technology, Zhengzhou 450001, China

²³Huangshan College, Huangshan 245000, China

²⁴Hunan Normal University, Changsha 410081, China

²⁵Hunan University, Changsha 410082, China

²⁶Indian Institute of Technology Madras, Chennai 600036, India

²⁷Indiana University, Bloomington, Indiana 47405, USA

^{28A}INFN Laboratori Nazionali di Frascati, INFN Laboratori Nazionali di Frascati, I-00044, Frascati, Italy

^{28B}INFN Laboratori Nazionali di Frascati, INFN Sezione di Perugia, I-06100, Perugia, Italy

^{28C}INFN Laboratori Nazionali di Frascati, University of Perugia, I-06100, Perugia, Italy

^{29A}INFN Sezione di Ferrara, INFN Sezione di Ferrara, I-44122, Ferrara, Italy

^{29B}INFN Sezione di Ferrara, University of Ferrara, I-44122, Ferrara, Italy

³⁰Inner Mongolia University, Hohhot 010021, China

³¹Institute of Modern Physics, Lanzhou 730000, China

³²Institute of Physics and Technology, Mongolian Academy of Sciences, Peace Avenue 54B, Ulaanbaatar 13330, Mongolia

³³Instituto de Alta Investigación, Universidad de Tarapacá, Casilla 7D, Arica 1000000, Chile

³⁴Jilin University, Changchun 130012, China

³⁵Johannes Gutenberg University of Mainz, Johann-Joachim-Becher-Weg 45, D-55099 Mainz, Germany

³⁶Joint Institute for Nuclear Research, 141980 Dubna, Moscow region, Russia

³⁷Justus-Liebig-Universität Giessen, II. Physikalisches Institut, Heinrich-Buff-Ring 16, D-35392 Giessen, Germany

³⁸Lanzhou University, Lanzhou 730000, China

³⁹Liaoning Normal University, Dalian 116029, China

⁴⁰Liaoning University, Shenyang 110036, China

⁴¹Nanjing Normal University, Nanjing 210023, China

⁴²Nanjing University, Nanjing 210093, China

⁴³Nankai University, Tianjin 300071, China

⁴⁴National Centre for Nuclear Research, Warsaw 02-093, Poland

- ⁴⁵North China Electric Power University, Beijing 102206, China
⁴⁶Peking University, Beijing 100871, China
⁴⁷Qufu Normal University, Qufu 273165, China
⁴⁸Renmin University of China, Beijing 100872, China
⁴⁹Shandong Normal University, Jinan 250014, China
⁵⁰Shandong University, Jinan 250100, China
⁵¹Shanghai Jiao Tong University, Shanghai 200240, China
⁵²Shanxi Normal University, Linfen 041004, China
⁵³Shanxi University, Taiyuan 030006, China
⁵⁴Sichuan University, Chengdu 610064, China
⁵⁵Soochow University, Suzhou 215006, China
⁵⁶South China Normal University, Guangzhou 510006, China
⁵⁷Southeast University, Nanjing 211100, China
⁵⁸State Key Laboratory of Particle Detection and Electronics, Beijing 100049, Hefei 230026, China
⁵⁹Sun Yat-Sen University, Guangzhou 510275, China
⁶⁰Suranaree University of Technology, University Avenue 111, Nakhon Ratchasima 30000, Thailand
⁶¹Tsinghua University, Beijing 100084, China
^{62A}Turkish Accelerator Center Particle Factory Group, Istinye University, 34010, Istanbul, Turkey
^{62B}Turkish Accelerator Center Particle Factory Group, Near East University, Nicosia, North Cyprus, 99138, Mersin 10, Turkey
⁶³University of Bristol, H H Wills Physics Laboratory, Tyndall Avenue, Bristol, BS8 1TL, UK
⁶⁴University of Chinese Academy of Sciences, Beijing 100049, China
⁶⁵University of Groningen, NL-9747 AA Groningen, The Netherlands
⁶⁶University of Hawaii, Honolulu, Hawaii 96822, USA
⁶⁷University of Jinan, Jinan 250022, China
⁶⁸University of Manchester, Oxford Road, Manchester, M13 9PL, United Kingdom
⁶⁹University of Muenster, Wilhelm-Klemm-Strasse 9, 48149 Muenster, Germany
⁷⁰University of Oxford, Keble Road, Oxford OX13RH, United Kingdom
⁷¹University of Science and Technology Liaoning, Anshan 114051, China
⁷²University of Science and Technology of China, Hefei 230026, China
⁷³University of South China, Hengyang 421001, China
⁷⁴University of the Punjab, Lahore-54590, Pakistan
^{75A}University of Turin and INFN, University of Turin, I-10125, Turin, Italy
^{75B}University of Turin and INFN, University of Eastern Piedmont, I-15121, Alessandria, Italy
^{75C}University of Turin and INFN, INFN, I-10125, Turin, Italy
⁷⁶Uppsala University, Box 516, SE-75120 Uppsala, Sweden
⁷⁷Wuhan University, Wuhan 430072, China
⁷⁸Yantai University, Yantai 264005, China
⁷⁹Yunnan University, Kunming 650500, China
⁸⁰Zhejiang University, Hangzhou 310027, China
⁸¹Zhengzhou University, Zhengzhou 450001, China
^aDeceased
^bAlso at the Moscow Institute of Physics and Technology, Moscow 141700, Russia
^cAlso at the Novosibirsk State University, Novosibirsk, 630090, Russia
^dAlso at the NRC "Kurchatov Institute", PNPI, 188300, Gatchina, Russia
^eAlso at Goethe University Frankfurt, 60323 Frankfurt am Main, Germany
^fAlso at Key Laboratory for Particle Physics, Astrophysics and Cosmology, Ministry of Education; Shanghai Key Laboratory for Particle Physics and Cosmology; Institute of Nuclear and Particle Physics, Shanghai 200240, China
^gAlso at Key Laboratory of Nuclear Physics and Ion-beam Application (MOE) and Institute of Modern Physics, Fudan University, Shanghai 200443, China
^hAlso at State Key Laboratory of Nuclear Physics and Technology, Peking University, Beijing 100871, China
ⁱAlso at School of Physics and Electronics, Hunan University, Changsha 410082, China
^jAlso at Guangdong Provincial Key Laboratory of Nuclear Science, Institute of Quantum Matter, South China Normal University, Guangzhou 510006, China
^kAlso at MOE Frontiers Science Center for Rare Isotopes, Lanzhou University, Lanzhou 730000, China
^lAlso at Lanzhou Center for Theoretical Physics, Lanzhou University, Lanzhou 730000, China
^mAlso at the Department of Mathematical Sciences, IBA, Karachi 75270, Pakistan
ⁿAlso at École Polytechnique Fédérale de Lausanne (EPFL), CH-1015 Lausanne, Switzerland
^oAlso at Helmholtz Institute Mainz, Staudinger Weg 18, D-55099 Mainz, Germany
^pAlso at Hangzhou Institute for Advanced Study, University of Chinese Academy of Sciences, Hangzhou 310024, China

Abstract: Using 20.3 fb^{-1} of e^+e^- annihilation data collected at a center-of-mass energy of 3.773 GeV with the BESIII detector, we report on an improved search for the radiative leptonic decay $D^+ \rightarrow \gamma e^+ \nu_e$. An upper limit on its partial branching fraction for photon energies $E_\gamma > 10 \text{ MeV}$ was determined to be 1.2×10^{-5} at a 90% confidence level; this excludes most current theoretical predictions. A sophisticated deep learning approach, which includes thorough validation and is based on the Transformer architecture, was implemented to efficiently distinguish the signal from massive backgrounds.

Keywords: charmed hadron, radiative leptonic decay, BESIII experiment, deep learning

DOI: 10.1088/1674-1137/adcd3

CSTR: 32044.14.ChinesePhysicsC.49083001

I. INTRODUCTION

The purely leptonic decays of charmed mesons, $D^+ \rightarrow l^+ \nu_l$ ($l = e, \mu, \tau$), offer an ideal laboratory for testing the Standard Model. These decays also offer one of the simplest and best understood probes of the $c \rightarrow d$ quark flavour-changing transition [1–4]. However, these decays are subject to helicity suppression, with decay rates proportional to the square of the lepton mass. Consequently, the $D^+ \rightarrow e^+ \nu_e$ decay rate is highly suppressed compared to its muonic [5, 6] and tauonic [5, 7] counterparts, with a branching fraction (BF) expected to be approximately 10^{-8} , beyond the current experimental sensitivity [8, 9].

In the radiative leptonic decay $D^+ \rightarrow \gamma e^+ \nu_e$, photon emission mitigates helicity suppression, with the strong interaction engaged solely in a single hadronic external state. Theoretically, its differential decay width can be expressed as a function of the photon energy E_γ in the rest frame of the D^+ meson [10] via

$$\frac{d\Gamma}{dE_\gamma}(D^+ \rightarrow \gamma l^+ \nu_l) = \frac{\alpha_{em} G_F^2 [F_V^2(E_\gamma) + F_A^2(E_\gamma)]}{6\pi^2} \times |V_{cd}|^2 E_\gamma^3 m_{D^+} \left(1 - \frac{2E_\gamma}{m_{D^+}}\right), \quad (1)$$

where α_{em} is the fine-structure constant, G_F is the Fermi coupling constant, $|V_{cd}|$ is the Cabibbo-Kobayashi-Maskawa matrix element [11, 12], m_{D^+} is the nominal mass of the D^+ meson [13], and F_V and F_A are the form factors characterizing the non-perturbative quantum chromodynamics (QCD) dynamics. Various theoretical models have been proposed to investigate the $D^+ \rightarrow \gamma e^+ \nu_e$ decay, including quark models [14–16], perturbative QCD [17], lattice QCD [18], and QCD factorization approaches [10, 19, 20]. Most theoretical predictions on its BF, $\mathcal{B}(D^+ \rightarrow \gamma e^+ \nu_e)$, are on the order of 10^{-5} , as summarized in Table 1.

The only experimental result on $D^+ \rightarrow \gamma e^+ \nu_e$ was reported from the BESIII experiment [21], based on 2.9 fb^{-1} of e^+e^- annihilation data taken at the center-of-mass energy $\sqrt{s} = 3.773 \text{ GeV}$. The upper limit on the partial BF of $D^+ \rightarrow \gamma e^+ \nu_e$ with $E_\gamma > 10 \text{ MeV}$ was determined to be 3.0×10^{-5} at 90% confidence level (C.L.), approaching the range of theoretical predictions [10, 16–20]. A larger dataset comprising 20.3 fb^{-1} of e^+e^- annihilation data recently collected at BESIII [22–24], which includes the previous 2.9 fb^{-1} data, provides an excellent opportunity to further constrain these theoretical models.

The major challenge in searching for $D^+ \rightarrow \gamma e^+ \nu_e$ is

the substantial background contamination from D^+ semileptonic decays, such as $D^+ \rightarrow \pi^0 e^+ \nu_e$, $D^+ \rightarrow K_L^0 e^+ \nu_e$, and $D^+ \rightarrow K_S^0 (\rightarrow \pi^0 \pi^0) e^+ \nu_e$. Photons originating from π^0 decays or long-lived neutral hadrons can deposit energy in the electromagnetic calorimeter, potentially mimicking the radiative photon signal. Conventional cut-based methods have struggled to establish effective discriminators to suppress these backgrounds, whose yields are two orders of magnitude greater than the potential signal.

An unprecedentedly powerful signal identification tool can be accomplished using deep learning, utilizing a deep neural network (DNN), to distinguish signals from backgrounds. Leveraging flexible data representation and modern algorithms, this method exhibits powerful capabilities in recognizing and interpreting underlying relationships and hidden patterns within the topological structure of e^+e^- annihilation events.

In this paper, we present an improved search for $D^+ \rightarrow \gamma e^+ \nu_e$ based on the analysis of the aforementioned 20.3 fb^{-1} data, enhancing signal sensitivity through a deep-learning-based signal identification method. Throughout this paper, charge conjugation is implied by default.

II. BESIII DETECTOR AND MONTE CARLO SIMULATION

The BESIII detector [25] records symmetric e^+e^- collisions provided by the BEPCII storage ring [26] in the center-of-mass energy range from 1.84 to 4.95 GeV, with a peak luminosity of $1.1 \times 10^{33} \text{ cm}^{-2} \text{ s}^{-1}$ achieved at $\sqrt{s} = 3.773 \text{ GeV}$. BESIII has collected large data samples in this energy region [27–29]. The cylindrical core of the BESIII detector covers 93% of the full solid angle and

Table 1. Theoretical predictions and experimental result for $\mathcal{B}(D^+ \rightarrow \gamma e^+ \nu_e)$.

Model	$\mathcal{B} (\times 10^{-5})$
Light front quark model [14]	0.69
Non-relativistic quark model [15]	0.46
Relativistic quark model [16]	3.34
Perturbative QCD [17]	8.2 ± 6.5
Lattice QCD [18]	0.09 ± 0.04
QCD factorization [19]	2.81
QCD factorization [20]	1.92
QCD factorization [10]	$(1.88^{+0.36}_{-0.29}, 2.31^{+0.65}_{-0.54})$
BESIII 2017 [21]	< 3.0

consists of a helium-based multilayer drift chamber (MDC), a time-of-flight system (TOF), and a CsI(Tl) electromagnetic calorimeter (EMC), which are all enclosed in a superconducting solenoidal magnet providing a 1.0 T magnetic field. The solenoid is supported by an octagonal flux-return yoke with resistive plate counter muon identification modules interleaved with steel. The charged-particle momentum resolution at 1 GeV/c is 0.5%, and the dE/dx resolution is 6% for electrons from Bhabha scattering. The EMC measures photon energies with a resolution of 2.5% (5%) at 1 GeV in the barrel (end cap) region. The time resolution in the plastic scintillator TOF barrel region is 68 ps, while that in the end cap region is 110 ps. The end cap TOF system was upgraded in 2015 using multigap resistive plate chamber technology, currently providing a time resolution of 60 ps, which benefits 85% of the data used in this analysis [30–32].

Monte Carlo (MC) simulated data samples produced with a GEANT4-based [33] software package, which includes the geometric description of the BESIII detector and its response, were used in this study to determine detection efficiencies and estimate backgrounds. A signal MC sample of the decay $D^+ \rightarrow \gamma e^+ \nu_e$ was simulated according to Eq. (1), where the form factors were taken from Ref. [20]. The minimum energy of the radiative photon was set at 10 MeV to avoid the infrared divergence for soft photons. In the simulation, we modeled the beam energy spread and initial state radiation (ISR) in the e^+e^- annihilations with the generator KKMC [34, 35]. The inclusive MC sample encompassed the production of $D\bar{D}$ pairs (including quantum coherence for the neutral D channels), non- $D\bar{D}$ decays of $\psi(3770)$, ISR production of the J/ψ and $\psi(3686)$ states, and continuum processes incorporated in KKMC [34, 35]. All particle decays were modeled with EVTGEN [36, 37] using BFs either taken from the Particle Data Group [13], when available, or otherwise estimated with LUNDCHARM [38, 39]. Final state radiation from charged final state particles was incorporated using the PHOTOS package [40].

III. INITIAL DATA ANALYSIS

Taking advantage of the D^+D^- pair production in e^+e^- annihilation at $\sqrt{s} = 3.773$ GeV, we employed a double-tag (DT) analysis method [41] to constrain the kinematics of $D^+ \rightarrow \gamma e^+ \nu_e$ and suppress non- D^+D^- backgrounds. The D^- meson was first reconstructed through six specific hadronic decay modes: $K^+\pi^-\pi^-$, $K^+\pi^-\pi^-\pi^0$, $K_S^0\pi^-$, $K_S^0\pi^-\pi^0$, $K_S^0\pi^+\pi^-\pi^-$, and $K^+K^-\pi^-$. Here, K_S^0 was reconstructed with a $\pi^+\pi^-$ pair, and π^0 was reconstructed from two photons. These decay modes are referred to as tag modes, and the selected events are called single-tag (ST) events. In the presence of the ST D^- meson, the signal decay $D^+ \rightarrow \gamma e^+ \nu_e$ was searched for within its recoil

system, with selected events referred to as DT events. The BF of the signal decay was determined from

$$\mathcal{B}_{\text{sig}} = \frac{N_{\text{DT}}}{\sum_i (N_{\text{ST}}^i \epsilon_{\text{ST}}^i / \epsilon_{\text{DT}}^i)}, \quad (2)$$

where N_{DT} represents the sum of DT yields for all tag modes, and N_{ST}^i , ϵ_{ST}^i , and ϵ_{DT}^i are the ST yield, ST efficiency, and DT efficiency for the tag mode i , respectively.

For reconstructing the ST D^- meson, charged tracks detected in the MDC were required to be within a polar angle (θ) range of $|\cos\theta| < 0.93$, where θ is defined with respect to the z -axis, which is the symmetry axis of the MDC. For charged tracks not originating from K_S^0 decays, the distance of closest approach to the interaction point (IP) was required to be less than 10 cm along the z -axis, V_z , and less than 1 cm in the transverse plane, V_{xy} . Particle identification (PID) for charged tracks combines measurements of the energy loss in the MDC (dE/dx) and the flight time in the TOF system to form likelihoods $\mathcal{L}(h)$ ($h = K, \pi$) for each hadron h hypothesis. The charged kaons or pions not originating from K_S^0 were required to satisfy $\mathcal{L}(K) > \mathcal{L}(\pi)$ or $\mathcal{L}(\pi) > \mathcal{L}(K)$, respectively.

The K_S^0 candidates were reconstructed from two oppositely charged tracks satisfying $V_z < 20$ cm. The two charged tracks were assigned as $\pi^+\pi^-$ without imposing further PID criteria. They were constrained to originate from a common vertex and required to have an invariant mass in the range of (487, 511) MeV/ c^2 corresponding to approximately $\pm 3\sigma$ of the detection resolution. The decay length of the K_S^0 candidate was required to be greater than twice the vertex resolution away from the IP.

Photon candidates were identified using showers in the EMC. The deposited energy of each shower was required to exceed 25 MeV in the barrel region ($|\cos\theta| < 0.80$) and 50 MeV in the end cap region ($0.86 < |\cos\theta| < 0.92$). To exclude showers that originated from charged tracks, the angle subtended by the EMC shower and the position of the closest charged track at the EMC were required to exceed 10 degrees as measured from the IP. To suppress electronic noise and showers unrelated to the event, the difference between the EMC time and the event start time was required to be within [0, 700] ns. The π^0 mesons were reconstructed using a kinematic fit from all combinations of two photon candidates by constraining their invariant mass to the nominal π^0 mass [13]. The invariant mass of two photons before the kinematic fit was required to be in the range of (115, 150) MeV/ c^2 . The combinations with both photons from end cap EMC regions were rejected because of poor resolution.

After selecting the component particles, we reconstructed the ST D^- meson using their combinations. Two kinematic variables, the energy difference ΔE , and the

beam-constrained mass M_{BC} were calculated for signal extraction as follows:

$$\Delta E = E_{D^-} - E_{\text{beam}}, \quad (3)$$

$$M_{BC} = \sqrt{E_{\text{beam}}^2/c^4 - |\vec{p}_{D^-}|^2/c^2}, \quad (4)$$

where E_{beam} is the beam energy, and \vec{p}_{D^-} and E_{D^-} are the momentum vector and energy of the D^- candidate in the e^+e^- rest frame, respectively. If multiple combinations were present in an event, the combination with the smallest $|\Delta E|$ value was retained for further analysis for each tag mode and charge. To suppress combinatorial backgrounds, mode-dependent requirements on ΔE were imposed on the accepted candidates within an approximate range of $\pm 3.5\sigma$ for the detection resolution, as listed in Table 2.

The ST yields were obtained through maximum likelihood fits to the M_{BC} distributions after applying the aforementioned requirements, as shown in Fig. 1. In each fit, the signal was described by the shape obtained from MC simulation, convolved with a double-Gaussian function to take into account resolution differences between data and MC simulation results. The background was described by an ARGUS function [42] with the endpoint fixed at the beam energy and other parameters left free. A signal region $M_{BC} \in (1.863, 1.877)$ MeV/ c^2 , corresponding to approximately $\pm 3\sigma$ of the detection resolution, was set to further reject the backgrounds. The ST efficiencies were estimated by analyzing the inclusive MC sample with the same method as in data, dividing the fitted yields by the numbers of generated events. Table 2 summarizes the ST yields in data and ST efficiencies for each tag mode.

The signal candidates for $D^+ \rightarrow \gamma e^+ \nu_e$ were selected from the remaining charged tracks and showers, excluding those associated with the ST D^- meson. We required only one track left with charge opposite to that of the ST D^- meson, following the same selection criteria as those in the tag side. This track was required to be identified as a positron combining the PID information from dE/dx, the TOF system, and the EMC, satisfying $\mathcal{L}(e) > 0.001$ and $\mathcal{L}(e)/[\mathcal{L}(e) + \mathcal{L}(\pi) + \mathcal{L}(K)] > 0.8$ for the combined confidence levels. We also required that at least one photon candidate satisfied the same selection criteria used in the tag side. If multiple photon candidates passed the selection, the most energetic one was chosen as the signal radiative photon. To improve the kinematic resolution of the positron, final-state-radiation recovery was performed by adding the momenta of any remaining photon candidates back to the reconstructed momentum of positron candidate if their opening angles with respect to the IP were less than 5° .

Table 2. ΔE requirements, ST yields in data, and ST and DT efficiencies for each tag mode in data. Note that the efficiencies do not include the BF's of subsequent π^0 and K_S^0 decays.

Tag mode	$\Delta E/\text{MeV}$	$N_{\text{ST}}^i (\times 10^3)$	$\epsilon_{\text{ST}}^i (\%)$	$\epsilon_{\text{DT}}^i (\%)$
$K^+ \pi^- \pi^-$	(-25, 24)	5552.8 ± 2.5	51.10	10.78
$K_S^0 \pi^-$	(-25, 26)	656.5 ± 0.8	51.42	10.69
$K^+ \pi^- \pi^- \pi^0$	(-57, 46)	1723.7 ± 1.8	24.40	5.42
$K_S^0 \pi^- \pi^0$	(-62, 49)	1442.4 ± 1.5	26.45	5.57
$K_S^0 \pi^- \pi^- \pi^+$	(-28, 27)	790.2 ± 1.1	29.59	6.62
$K^+ K^- \pi^-$	(-24, 23)	481.4 ± 0.9	40.91	8.96

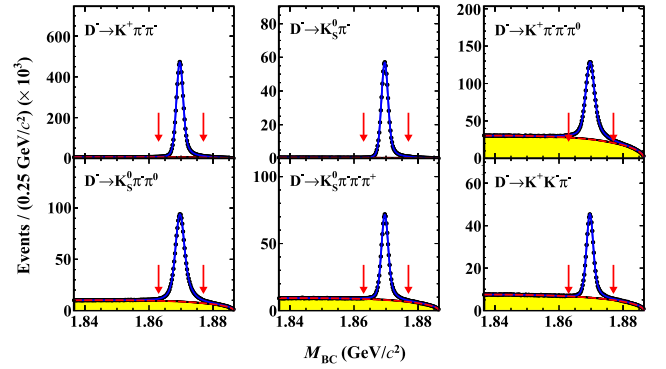


Fig. 1. (color online) Fits to the M_{BC} distributions of ST D^- candidates for each tag mode in data. The black dots with error bars represent data. The blue curves are the fit results. The red dotted curves are the fitted combinatorial background shapes. The yellow histograms are the MC simulated background scaled to the luminosity of data. The red arrows indicate the signal region.

To derive information about the missing neutrino, a kinematic observable U_{miss} was defined as

$$U_{\text{miss}} = E_{\text{miss}} - |\vec{p}_{\text{miss}}|c, \quad (5)$$

where E_{miss} and \vec{p}_{miss} represent the total energy and momentum vector of all missing particles in the event. The missing energy was calculated as $E_{\text{miss}} = E_{\text{beam}} - E_{e^+} - E_{\gamma}$, where E_{e^+} and E_{γ} are the energies of signal positron and photon, respectively. The missing momentum was calculated as $\vec{p}_{\text{miss}} = \vec{p}_{D^+} - \vec{p}_{e^+} - \vec{p}_{\gamma}$, where \vec{p}_{D^+} , \vec{p}_{e^+} , and \vec{p}_{γ} are the momenta of signal D^+ meson, positron, and photon, respectively. The D^+ momentum was further constrained as $\vec{p}_{D^+} = -\frac{\vec{p}_{\text{ST}}}{|\vec{p}_{\text{ST}}|} \sqrt{E_{\text{beam}}^2 - m_{D^+}^2}$, where \vec{p}_{ST} is the momentum of the ST D^- meson. The consequent analysis was performed within $U_{\text{miss}} \in (-0.2, 0.2)$ GeV.

We also explored $D^+ \rightarrow \pi^0 e^+ \nu_e$ as a validation channel in this study. For reconstructing $D^+ \rightarrow \pi^0 e^+ \nu_e$ events, additional DT selection criteria were applied after those mentioned above. At least one π^0 candidate was required,

and the one with minimum χ^2 from the kinematic fit was chosen as the signal π^0 candidate. Another kinematic observable, U'_{miss} , was defined as

$$U'_{\text{miss}} = E'_{\text{miss}} - \left| \vec{p}'_{\text{miss}} \right| c, \quad (6)$$

where $E'_{\text{miss}} = E_{\text{beam}} - E_{e^+} - E_{\pi^0}$ and $\vec{p}'_{\text{miss}} = \vec{p}_{D^+} - \vec{p}_{e^+} - \vec{p}_{\pi^0}$ were calculated using the energy and momentum of the signal π^0 candidate, respectively.

Figure 2(a) presents the U_{miss} distributions for both data and inclusive MC samples after applying the aforementioned selections. The major backgrounds are from $D^+ \rightarrow \pi^0 e^+ \nu_e$, $D^+ \rightarrow K_L^0 e^+ \nu_e$, and $D^+ \rightarrow K_S^0 (\rightarrow \pi^0 \pi^0) e^+ \nu_e$. Notably, the $D^+ \rightarrow \pi^0 e^+ \nu_e$ background exhibits a non-trivial shape within the signal region. The high background level makes it difficult to reliably extract the signal yield from the U_{miss} distribution with adequate sensit-

ivity, thereby requiring further signal identification treatments, as explained below.

IV. DEEP-LEARNING-BASED SIGNAL IDENTIFICATION

The main challenge in distinguishing signals from massive backgrounds lies in extracting distinctive features from the data. Notably, the shower patterns observed in the EMC provide key information for this task. Background events involving a π^0 typically result in a higher number of photon candidates than the signal, whereas K_L^0 -induced showers often exhibit more dispersed cluster shapes compared to those from photons [43]. Additionally, the kinematics of the particles, influenced by the unique phase spaces and dynamics of their decays, offer another aspect of differentiation. Conventional cut-based methods characterize such distinctions via hand-crafted variables derived from practical understanding of the involved physics, such as the number of π^0 -like photon combinations, lateral moment of photon candidates [21], and χ^2 values from kinematic fits under specific final-state hypotheses [44]. In contrast, deep learning methods aim to process minimally refined data at the level of fundamental detector responses to the penetrations of the final state particles. A DNN is expected to automatically explore underlying correlations and recognize distinctive information beyond prior knowledge.

In this study, the dataset for DNN training was constructed by randomly shuffling signal and background events sourced from relevant MC samples. The events were categorized into three groups with equal statistics: $D^+ \rightarrow \gamma e^+ \nu_e$ signal, $D^+ \rightarrow \pi^0 e^+ \nu_e$ background, and other inclusive backgrounds. The training dataset contained approximate 3.3 million events in total, with 80% used for training and the remaining 20% reserved for validation. The DNN input information from an event included all charged tracks reconstructed in the MDC and isolated showers clustered in the EMC. These particles were organized as a *point cloud* [45] structure, i.e., an unordered and variable-sized set of points in a high-dimensional feature space. For each charged track, the features comprised the azimuthal and polar angles in the center-of-mass frame, charge, magnitude of momentum, and parameters characterizing its helical trajectory in the MDC. Additionally, low-level measurements from the MDC, TOF, and EMC were incorporated as implicit information for particle identification and reconstruction quality. For each shower, the features comprised the azimuthal and polar angles, energy deposition, count of fired crystals, time measurement, and parameters describing its expansion scope among nearby crystals. A full list of input features is provided in Table 3; these features were found to be consistent between data and MC simulation results.

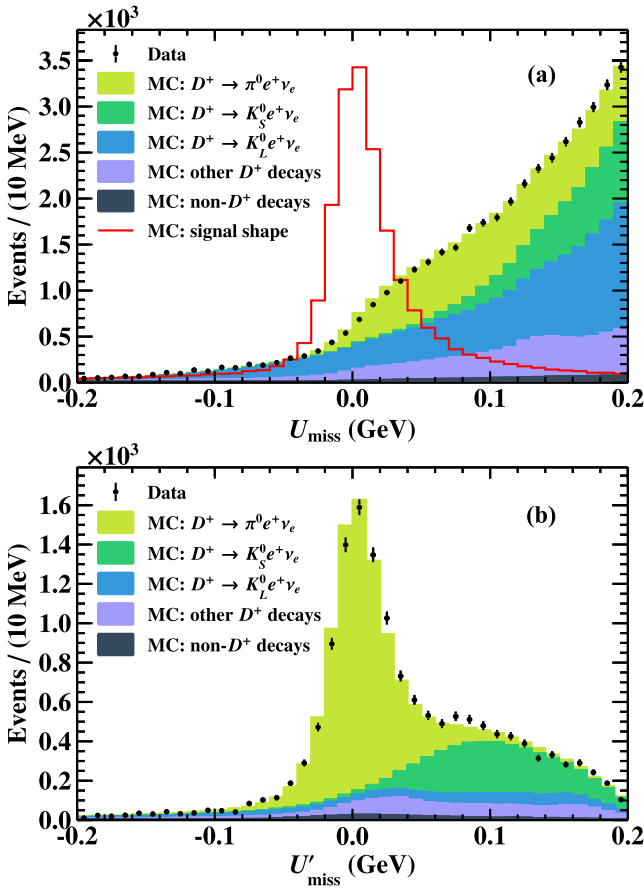


Fig. 2. (color online) (a) U_{miss} distribution of the signal decay $D^+ \rightarrow \gamma e^+ \nu_e$ and (b) U'_{miss} distribution of the validation channel $D^+ \rightarrow \pi^0 e^+ \nu_e$ after DT selection. The black dots with error bars represent data. The histograms with filled colors represent different background components in the inclusive MC sample. The red hollow histogram indicates an arbitrarily scaled signal shape.

Table 3. Input particle feature variables and their availability in tracks and showers. If measurements were unavailable from the detector readouts, the default value was set to zero.

Variable	Definition	Track	Shower
θ	azimuthal angle	✓	✓
ϕ	polar angle	✓	✓
p	momentum magnitude	✓	–
charge	electric charge	✓	–
d_p	distance in the $x-y$ plane from the point of closest approach (POCA) of the track to the IP	✓	–
d_Z	distance along z -axis from the POCA of the track to the IP	✓	–
ϕ_0	azimuthal angle of the track at the POCA	✓	–
κ	scaled inverse of the momentum of the track	✓	–
$\tan \lambda$	tangent value of the angle of the track at the POCA with respect to the $x-y$ plane	✓	–
$\chi_{dE/dx}(e)$	deviation in dE/dx measurement of the track from the anticipated positron value	✓	–
$\chi_{dE/dx}(\pi)$	deviation in dE/dx measurement of the track from the anticipated pion value	✓	–
$\chi_{dE/dx}(K)$	deviation in dE/dx measurement of the track from the anticipated kaon value	✓	–
$\chi_{TOF}(\pi)$	deviation in TOF measurement of the track from the anticipated pion value	✓	–
$\chi_{TOF}(K)$	deviation in TOF measurement of the track from the anticipated kaon value	✓	–
Q_{TOF}	pulse height of the track in TOF corresponding to its deposited energy	✓	–
β_{TOF}	velocity of the track measured by TOF	✓	–
E_{raw}	total deposited energy in EMC	✓	✓
E_{seed}	deposited energy of the crystal at the shower center	✓	✓
$E_{3 \times 3}$	sum of energies of 3×3 crystal matrices surrounding the shower center	✓	✓
$E_{5 \times 5}$	sum of energies of 5×5 crystal matrices surrounding the shower center	✓	✓
N_{hits}	count of fired crystals in the shower	✓	✓
time	EMC time measurement	✓	✓
secondary moment	shower expansion parameter defined as $\sum_i E_i r_i^2 / \sum_i E_i$	✓	✓
lateral moment	shower expansion parameter defined as $\sum_{i=3}^n E_i r_i^2 / (E_1 r_0^2 + E_2 r_0^2 + \sum_{i=3}^n E_i r_i^2)$	✓	✓
A_{20} moment	shower expansion parameter defined as $\sum_i \frac{E_i}{E_{tot}} f_{2,0}(\frac{r_i}{R_0})$, $f_{2,0}(x) = 2x^2 - 1$	✓	✓
A_{42} moment	same but defined as $\left \sum_i \frac{E_i}{E_{tot}} f_{4,2}(\frac{r_i}{R_0}) e^{2i\phi} \right $, $f_{4,2}(x) = 4x^4 - 3x^2$	✓	✓

The architecture of the DNN used in this study largely inherits from the Particle Transformer (ParT) [46], with adaptations tailored for the BESIII experiment. A key innovation of the ParT is the injection of particle physics knowledge into the Transformer network [47], where a set of pairwise interaction features are calculated using the energy-momentum vectors for each pair of particles and incorporated as biases \mathbf{U} in the self-attention mechanism. This treatment efficiently captures the kinematic relationships between particles, significantly improving the ParT performance. For the BESIII application, we considered its unique properties, such as a purely spherical coordinate system and energy-momentum conservation in 3D space, by designing a new set of pairwise interaction features \mathbf{U}_{BES} defined as

$$\mathbf{U}_{\text{BES}} = \begin{cases} 1 - \cos \theta_{a,b}, \\ \min(E_a, E_b) (1 - \cos \theta_{a,b}), \\ \min(E_a, E_b) / (E_a + E_b), \\ (E_a + E_b)^2 - \|\vec{p}_a + \vec{p}_b\|^2, \end{cases} \quad (7)$$

where E_a and E_b are the energies of the two particles, \vec{p}_a and \vec{p}_b are their momentum vectors, and $\theta_{a,b}$ is the opening angle between these vectors in the center-of-mass frame. For the model hyperparameters, this adaptation includes four particle attention blocks and two class attention blocks. It uses a particle embedding encoded from the input particle features via a 3-layer multilayer perceptron with 128, 256, and 128 nodes in each layer and

an interaction embedding encoded from the input pairwise features using a 4-layer pointwise 1D convolution with 64, 64, 64, and 8 channels. A dropout rate of 0.1 was applied to prevent overfitting.

The training of the DNN was performed on the aforementioned dataset for 50 epochs with a batch size of 512 and an initial learning rate of 0.001. An additional treatment was employed during training to address the potential correlation between the DNN output and the U_{miss} distribution, which could inadvertently create signal-like structures in the U_{miss} distribution of remaining background events after applying the selection criteria on the DNN output [48–51]. To decouple the DNN output from the U_{miss} observable, we employed an iterative approach by assigning a weight $\omega(U_{\text{miss}})$ to each background event which adjusts its contribution to the loss function. Events with higher weights have a greater impact on the loss function, which means that they are better classified during training. The weight $\omega_i^j(U_{\text{miss}}^j)$ for an event j in the i -th iteration is calculated as

$$\omega_i^j(U_{\text{miss}}^j) = \omega_{i-1}^j(U_{\text{miss}}^j) \left[\frac{p_{i-1}^{\text{BKG}}(U_{\text{miss}})}{p_{\text{orig}}^{\text{BKG}}(U_{\text{miss}})} \bigg|_{U_{\text{miss}}=U_{\text{miss}}^j} \right], \quad (8)$$

where $\omega_0^j(U_{\text{miss}}^j) = 1$, $p_{i-1}^{\text{BKG}}(U_{\text{miss}})$ represents the normalized probability density function for the remaining background shape after the $(i-1)$ -th iteration, and $p_{\text{orig}}^{\text{BKG}}(U_{\text{miss}})$ denotes the original background shape before applying the DNN output veto. For each iteration, the DNN was re-trained, and both $p_{i-1}^{\text{BKG}}(U_{\text{miss}})$ and $\omega_i^j(U_{\text{miss}}^j)$ were updated. Intuitively, the process converged when $p_{i-1}^{\text{BKG}}(U_{\text{miss}})$ approached $p_{\text{orig}}^{\text{BKG}}(U_{\text{miss}})$, resulting in a trivial background shape that facilitates signal extraction. In practice, as shown in Fig. 3, this iterative approach partially corrects the $D^+ \rightarrow \pi^0 e^+ \nu_e$ background shape while successfully retrieving the original one for other inclusive background shapes. This result demonstrates both its effectiveness and limitations in addressing the mass correlation issue. Furthermore, another machine-learning technique called *model ensemble* was employed. With some randomness factors incorporated in the training, such as network initialization, batch processing sequence, and dropout [52], we trained a total of 20 DNNs in parallel in each iteration. The outputs of these DNNs were averaged for each event during inference, creating an ensemble DNN that offers better robustness and generalization than any single DNN model.

The DNN output assigns three scores in the range [0, 1] to each event, reflecting the probabilities of the event belonging to the signal, $D^+ \rightarrow \pi^0 e^+ \nu_e$ background, and other background categories. Given that the sum of the three scores always equals one, only two of them are independent. As the final step in the event selection, we re-

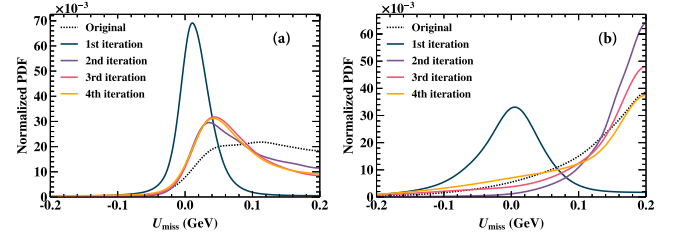


Fig. 3. (color online) Normalized (a) $D^+ \rightarrow \pi^0 e^+ \nu_e$ and (b) other inclusive background shapes in the U_{miss} distribution during the iteration process.

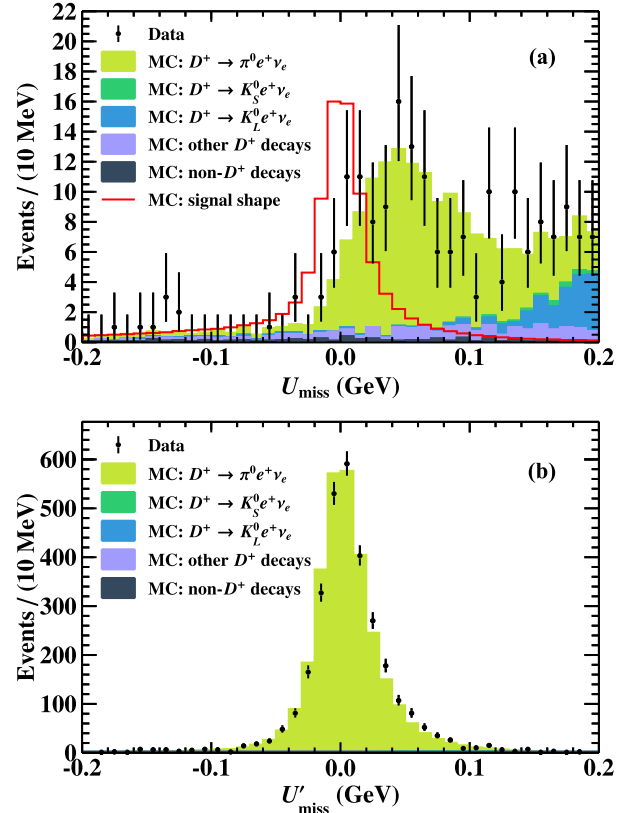


Fig. 4. (color online) (a) U_{miss} distribution of the signal decay $D^+ \rightarrow \gamma e^+ \nu_e$ and (b) U'_{miss} distribution of the validation decay $D^+ \rightarrow \pi^0 e^+ \nu_e$ after the DNN vetoes. The black dots with error bars represent data. The histograms with filled colors represent different background components in the inclusive MC sample. The red hollow histogram indicates an arbitrarily scaled signal shape.

quired the score for the $D^+ \rightarrow \pi^0 e^+ \nu_e$ background to be less than 0.15 and that for other backgrounds to be less than 0.05. These cut values were optimized using the Punzi significance metric, $\epsilon/(1.5 + \sqrt{B})$ [53], where ϵ represents the signal efficiency and B is the expected background yield. Figure 4(a) shows the U_{miss} distribution after implementing the deep learning approach. The backgrounds were reduced by more than two orders of magnitude at the cost of approximately two-thirds of the signal efficiency, significantly enhancing the sensitivity of

the signal search.

V. SIGNAL EXTRACTION

According to Eq. (2), the DT efficiencies for each tag mode, ϵ_{DT}^i , were estimated using signal MC samples; they are summarized in Table 2. To obtain the DT yield N_{DT} in data, a maximum likelihood fit was performed on the U_{miss} distribution combining all the tag modes. The fit included three components, namely the signal, $D^+ \rightarrow \pi^0 e^+ \nu_e$ background, and other backgrounds. The shapes for these components were taken from the corresponding MC simulations, and their yields were all floated in the fit. The fit resulted in $N_{\text{DT}} = 12.2 \pm 8.6$ and $\mathcal{B}(D^+ \rightarrow \gamma e^+ \nu_e) = (0.54 \pm 0.38) \times 10^{-5}$, as shown in Fig. 5(a), where the uncertainties are statistical only. Given that no significant signal was observed, an upper limit on the signal BF was set after accounting for all systematic uncertainties.

VI. VALIDATION

A common concern in adopting the deep learning method in particle physics experiments is the coupling between potential analysis biases and the sophisticated DNN structure, which makes these biases difficult to validate, quantify, and calibrate. The extensive and diverse datasets collected at BESIII facilitate various control samples in data to investigate these issues. In this study, our primary background process $D^+ \rightarrow \pi^0 e^+ \nu_e$ served as a natural control sample. By partially reversing the DNN vetoes, i.e., to require the score for the $D^+ \rightarrow \pi^0 e^+ \nu_e$ background to be *greater* than 0.15 while keeping the score for other backgrounds below 0.05, we could isolate a $D^+ \rightarrow \pi^0 e^+ \nu_e$ sample with a purity exceeding 98% and measure its absolute BF. Figures 2(b) and 4(b) show the U'_{miss} distributions before and after applying the partially reversed DNN vetoes, with significant subtraction of backgrounds other than $D^+ \rightarrow \pi^0 e^+ \nu_e$.

To measure the absolute BF of $D^+ \rightarrow \pi^0 e^+ \nu_e$, we used the value of ϵ_{DT}^i estimated from MC simulations and extracted N_{DT} via the maximum likelihood fit shown in Fig. 5(b). In the fit, the $D^+ \rightarrow \pi^0 e^+ \nu_e$ signal was modeled using the MC simulated shape convolved with a Gaussian resolution function. The other background component was described using the inclusive MC shape with the yield floated. The final fit to all data resulted in $N_{\text{DT}} = 3004 \pm 59$ and $\mathcal{B}(D^+ \rightarrow \pi^0 e^+ \nu_e) = (3.629 \pm 0.071) \times 10^{-3}$, where the uncertainty was statistical only. This result is consistent with previous BESIII measurements, $(3.63 \pm 0.08_{\text{stat.}} \pm 0.05_{\text{syst.}}) \times 10^{-3}$ [54], based on approximately one seventh of full data, thereby validating the reliability of our DNN method. The residual deviations were considered a source of systematic uncertainty, as detailed in the next section.

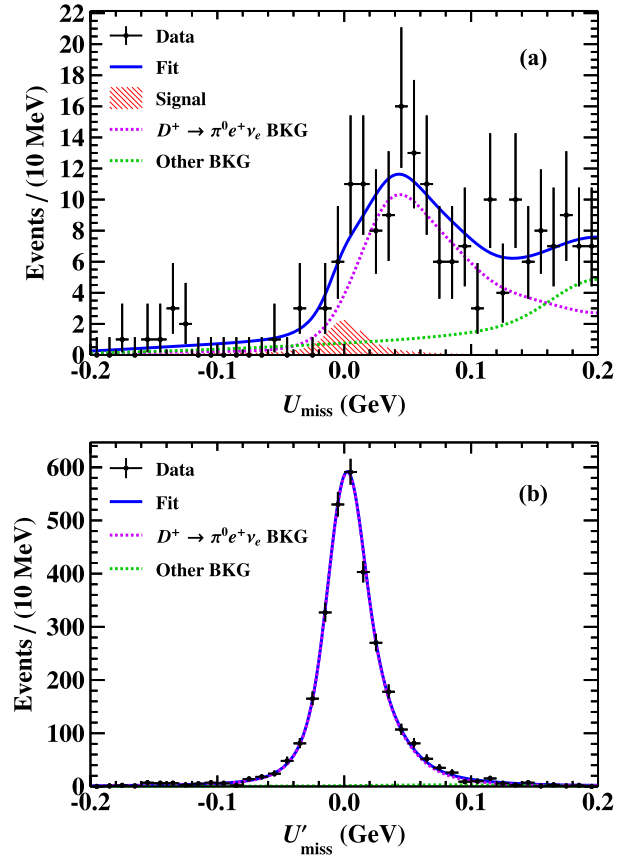


Fig. 5. (color online) Fits to (a) the U_{miss} distribution of the signal decay $D^+ \rightarrow \gamma e^+ \nu_e$ and (b) U'_{miss} distribution of the validation decay $D^+ \rightarrow \pi^0 e^+ \nu_e$. The points with error bars represent data. The blue line represents the fitted curve. The red dashed area represents a signal component, and other dashed lines represent background components.

VII. SYSTEMATIC UNCERTAINTIES

Systematic uncertainties in BF determination stem from various sources; many of them are related to the ST selection being canceled, benefiting from the DT technique. The remaining systematic sources can be grouped into two categories: multiplicative uncertainties, which affect the efficiency, and additive uncertainties, which impact the signal yield. These two types of uncertainties contribute to the upper limit of the BF through different approaches.

The multiplicative uncertainty sources include the ST yield, positron tracking, positron PID, photon reconstruction, MC model, and DNN vetoes, as summarized in Table 4. The uncertainty due to the ST yield was estimated by varying the descriptions of signal and background components in the M_{BC} fits and was set to 0.3%. A control sample of radiative Bhabha scattering events was used to study the position tracking and PID uncertainties, and the values for both were set to 1.0% [55]. The photon reconstruction uncertainty was set to 1.0%

Table 4. Multiplicative systematic uncertainties.

Source	Size (%)
ST yield	0.3
Positron tracking	1.0
Positron PID	1.0
Photon reconstruction	1.0
MC model	9.1
DNN vetoes	5.8
Total	10.9

using a control sample of $J/\psi \rightarrow \pi^+ \pi^- \pi^0$, $\pi^0 \rightarrow \gamma\gamma$ [56]. The uncertainty related to MC modeling was defined as the difference between the signal efficiencies of the nominal MC model and an alternative single-pole model [19]; it was set to 9.1%.

Special consideration was given to systematic uncertainties related to the DNN vetoes [57]. Following some frontier surveys [13, 58], we considered two primary uncertainty sources: *model uncertainty* and *domain shift*. Model uncertainty arises from our limited knowledge of the best model and was quantified by the relative shift in signal efficiency across the 20 DNNs trained during the model ensemble process. The standard deviation of these efficiencies, divided by their average, 5.3%, was taken as the corresponding systematic uncertainty. Domain shift describes the mismatch between datasets for training and inference, reflecting potential data-MC inconsistencies. This uncertainty was evaluated using the control sample of $D^+ \rightarrow \pi^0 e^+ \nu_e$ described in Section VI, with the deviation between our BF measurements and previous BESIII measurements [54] calculated to be 2.2%, combining the center value shift and 1σ statistical uncertainty. In total, the multiplicative systematic uncertainty was determined to be 10.9% by adding the above sources in quadrature.

The additive systematic uncertainties arise from the signal, $D^+ \rightarrow \pi^0 e^+ \nu_e$ background, and other background shapes used in the DT fit. These effects were evaluated by testing alternative descriptions of the shapes. One variation is in using parameterized functions, where the signal and $D^+ \rightarrow \pi^0 e^+ \nu_e$ background shapes were modeled by double-Gaussian functions, and the other background shape was modeled by a third-order Chebyshev polynomial. Another change was the use of MC-simulated shapes before the final iteration of the mass decorrelation process as well as across the 20 DNN predictions in the model ensemble process.

VIII. RESULTS

Given that no significant signal was observed in data, the upper limit on $\mathcal{B}(D^+ \rightarrow \gamma e^+ \nu_e)$ was set using a

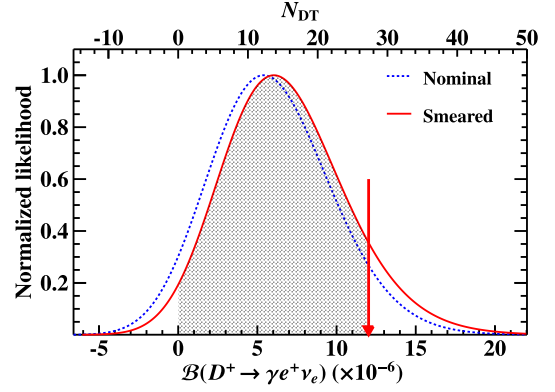


Fig. 6. (color online) Normalized likelihood distributions before and after incorporating the multiplicative and additive systematic uncertainties. The blue dashed line represents the initial distribution, whereas the red solid line represents the distribution with systematic uncertainties considered. The red arrow indicates the final upper limit.

Bayesian method described in Ref. [59]. We performed a series of maximum likelihood fits as described in Section V, with the signal yield N_{DT} fixed to each scanned value. The corresponding maximum likelihood values were used to construct a discrete likelihood distribution, $\mathcal{L}(\mathcal{B}_{sig})$. The systematic uncertainties were incorporated in two steps: first, the additive uncertainties were addressed by varying the DT fit method, with the most conservative upper limit retained. Next, the multiplicative uncertainties were considered by smearing the likelihood distribution as follows [60]:

$$\mathcal{L}'(\mathcal{B}_{sig}) \propto \int_0^1 \mathcal{L}\left(\mathcal{B}_{sig} \cdot \frac{\epsilon}{\epsilon_0}\right) e^{-\frac{(\epsilon - \epsilon_0)^2}{2\sigma_\epsilon^2}} d\epsilon, \quad (9)$$

where ϵ_0 is the nominal signal efficiency, and σ_ϵ is the multiplicative uncertainty corresponding to the efficiency value. By integrating the $\mathcal{L}'(\mathcal{B}_{sig})$ curve up to 90% of the area for $N_{DT} > 0$ and calculating the corresponding BF using Eq. (2), we set the upper limit on the BF of $D^+ \rightarrow \gamma e^+ \nu_e$ at 90% C.L. to be 1.2×10^{-5} , as shown in Fig. 6.

IX. SUMMARY

We conducted an improved search for the radiative leptonic decay $D^+ \rightarrow \gamma e^+ \nu_e$ using 20.3 fb⁻¹ of e^+e^- collision data taken at $\sqrt{s} = 3.773$ GeV with the BESIII detector. Our investigation does not reveal a significant signal but establishes an upper limit of 1.2×10^{-5} on its BF with a radiative photon energy above 10 MeV, at 90% C.L. This result excludes most existing theoretical predictions [10, 16–20], thereby indicating the necessity for further investigation of the decay mechanism. The key advancement of this study is the application of a novel deep

learning approach, which effectively distinguishes signals from massive backgrounds. Our results showcase the potential and broad applicability of deep learning techniques in particle physics research.

ACKNOWLEDGEMENTS

The BESIII Collaboration thanks the staff of BEPCII and the IHEP computing center for their strong support.

References

- [1] D. Silverman and H. Yao, *Phys. Rev. D* **38**, 214 (1988)
- [2] J. L. Rosner, *Phys. Rev. D* **42**, 3732 (1990)
- [3] C. H. Chang and Y. Q. Chen, *Phys. Rev. D* **46**, 3845 (1992) [Erratum: *Phys. Rev. D* **50**, 6013 (1994)]
- [4] C. H. Chang and Y. Q. Chen, *Phys. Rev. D* **49**, 3399 (1994)
- [5] Y. S. Amhis *et al.* (HFLAV Collaboration), *Phys. Rev. D* **107**, 052008 (2023), arXiv: 2206.07501[hep-ex]
- [6] M. Ablikim *et al.* (BESIII Collaboration), *Phys. Rev. D* **89**, 051104 (2014), arXiv: 1312.0374[hep-ex]
- [7] M. Ablikim *et al.* (BESIII Collaboration), *Phys. Rev. Lett.* **123**, 211802 (2019), arXiv: 1908.08877[hep-ex]
- [8] B. I. Eisenstein *et al.* (CLEO Collaboration), *Phys. Rev. D* **78**, 052003 (2008), arXiv: 0806.2112[hep-ex]
- [9] M. Ablikim *et al.* (BESIII), (2025), arXiv: 2501.04760[hep-ex]
- [10] L. S. Lu, *Chin. Phys. C* **45**, 073101 (2021), arXiv: 2104.01562[hep-ph]
- [11] N. Cabibbo, *Phys. Rev. Lett.* **10**, 531 (1963)
- [12] M. Kobayashi and T. Maskawa, *Prog. Theor. Phys.* **49**, 652 (1973)
- [13] S. Navas *et al.* (Particle Data Group), *Phys. Rev. D* **110**, 030001 (2024)
- [14] C. Q. Geng, C. C. Lih, and W. M. Zhang, *Mod. Phys. Lett. A* **15**, 2087 (2000), arXiv: hep-ph/0012066
- [15] C. D. Lu and G. L. Song, *Phys. Lett. B* **562**, 75 (2003), arXiv: hep-ph/0212363
- [16] N. Barik, S. Naimuddin, and P. C. Dash, *Int. J. Mod. Phys. A* **24**, 2335 (2009)
- [17] G. P. Korchemsky, D. Pirjol, and T. M. Yan, *Phys. Rev. D* **61**, 114510 (2000), arXiv: hep-ph/9911427
- [18] A. Desiderio, R. Frezzotti, M. Garofalo *et al.*, *Phys. Rev. D* **103**, 014502 (2021)
- [19] J. C. Yang and M. Z. Yang, *Nucl. Phys. B* **889**, 778 (2014), arXiv: 1409.0358[hep-ph]
- [20] J. C. Yang and M. Z. Yang, *Nucl. Phys. B* **914**, 301 (2017), arXiv: 1604.08300[hep-ph]
- [21] M. Ablikim *et al.* (BESIII Collaboration), *Phys. Rev. D* **95**, 071102 (2017), arXiv: 1702.05837[hep-ex]
- [22] M. Ablikim *et al.* (BESIII Collaboration), *Chin. Phys. C* **37**, 123001 (2013), arXiv: 1307.2022[hep-ex]
- [23] M. Ablikim *et al.* (BESIII Collaboration), *Phys. Lett. B* **753**, 629 (2016) [Erratum: *Phys. Lett. B* **812**, 135982 (2021)], arXiv: 1507.08188[hep-ex]
- [24] M. Ablikim *et al.* (BESIII Collaboration), *Chin. Phys. C* **48**, 1 (2024), arXiv: 2406.05827[hep-ex]
- [25] M. Ablikim *et al.* (BESIII Collaboration), *Nucl. Instrum. Meth. A* **614**, 345 (2010), arXiv: 0911.4960[physics.ins-det]
- [26] C. Yu *et al.*, in *Proceedings of International Particle Accelerator Conference (IPAC'16)*, Busan, Korea, 2016, Doi: 10.18429/JACoW-IPAC2016-TUYA01
- [27] M. Ablikim *et al.* (BESIII Collaboration), *Chin. Phys. C* **44**, 040001 (2020), arXiv: 1912.05983[hep-ex]
- [28] J. Lu, Y. Xiao, and X. Ji, *Radiat. Detect. Technol. Methods* **4**, 1 (2020)
- [29] J. W. Zhang *et al.*, *Radiat. Detect. Technol. Methods* **6**, 289 (2022)
- [30] X. Li *et al.*, *Radiat. Detect. Technol. Methods* **1**, 13 (2017)
- [31] Y. X. Guo *et al.*, *Radiat. Detect. Technol. Methods* **1**, 15 (2017)
- [32] P. Cao *et al.*, *Nucl. Instrum. Meth. A* **953**, 163053 (2020)
- [33] S. Agostinelli *et al.* (GEANT4 Collaboration), *Nucl. Instrum. Meth. A* **506**, 250 (2003)
- [34] S. Jadach, B. F. L. Ward, and Z. Was, *Comput. Phys. Commun.* **130**, 260 (2000), arXiv: hep-ph/9912214
- [35] S. Jadach, B. F. L. Ward, and Z. Was, *Phys. Rev. D* **63**, 113009 (2001), arXiv: hep-ph/0006359
- [36] D. J. Lange, *Nucl. Instrum. Meth. A* **462**, 152 (2001)
- [37] R. G. Ping, *Chin. Phys. C* **32**, 599 (2008)
- [38] J. C. Chen, G. S. Huang, X. R. Qi *et al.*, *Phys. Rev. D* **62**, 034003 (2000)
- [39] R. L. Yang, R. G. Ping, and H. Chen, *Chin. Phys. Lett.* **31**, 061301 (2014)
- [40] E. Barberio, B. van Eijk, and Z. Was, *Comput. Phys. Commun.* **66**, 115 (1991)
- [41] R. M. Baltrusaitis *et al.* (MARK-III Collaboration), *Phys. Rev. Lett.* **56**, 2140 (1986)
- [42] H. Albrecht *et al.* (ARGUS Collaboration), *Phys. Lett. B* **241**, 278 (1990)
- [43] Z. J. Li, M. K. Yuan, Y. X. Song *et al.*, *Front. Phys. (Beijing)* **19**, 64201 (2024), arXiv: 2404.07951[physics.data-an]
- [44] M. Ablikim *et al.* (BESIII Collaboration), *Phys. Rev. D* **99**, 072002 (2019), arXiv: 1902.03351[hep-ex]
- [45] H. Qu and L. Gouskos, *Phys. Rev. D* **101**, 056019 (2020), arXiv: 1902.08570[hep-ph]
- [46] H. Qu, C. Li, and S. Qian, in *International Conference on Machine Learning* (PMLR, 2022) pp. 18281–18292
- [47] . Vaswani, N. Shazeer, N. Parmar *et al.*, in *Advances in Neural Information Processing Systems*, Vol. 30 (2017).
- [48] J. Dolen, P. Harris, S. Marzani *et al.*, *JHEP* **05**, 156 (2016), arXiv: 1603.00027[hep-ph]
- [49] C. Englert, P. Galler, P. Harris *et al.*, *Eur. Phys. J. C* **79**, 4 (2019), arXiv: 1807.08763[hep-ph]
- [50] G. Kasieczka and D. Shih, *Phys. Rev. Lett.* **125**, 122001 (2020), arXiv: 2001.05310[hep-ph]
- [51] O. Kitouni, B. Nachman, C. Weisser *et al.*, *JHEP* **21**, 070 (2020), arXiv: 2010.09745[hep-ph]
- [52] N. Srivastava, G. Hinton, A. Krizhevsky *et al.*, *Journal of Machine Learning Research* **15**, 1929 (2014)
- [53] G. Punzi, eConf **C030908**, MODT002, (2003), arXiv: physics/0308063
- [54] M. Ablikim *et al.* (BESIII Collaboration), *Phys. Rev. D* **96**, 012002 (2017), arXiv: 1703.09084[hep-ex]
- [55] M. Ablikim *et al.* (BESIII Collaboration), *Phys. Rev. Lett.* **122**, 121801 (2019), arXiv: 1901.02133[hep-ex]
- [56] M. Ablikim *et al.* (BESIII Collaboration), *Phys. Rev. D* **83**, 112005 (2011), arXiv: 1103.5564[hep-ex]
- [57] P. Shanahan *et al.*, in *Proceedings of the 2021 US Community Study on the Future of Particle Physics*, (2022), arXiv: 2209.07559[physics.comp-ph]
- [58] T. Y. Chen, B. Dey, A. Ghosh, M. Kagan, B. Nord, and N. Ramachandra, in *Proceedings of the 2021 US Community Study on the Future of Particle Physics*, (2022), arXiv: 2208.03284[hep-ex]
- [59] K. Stenson, (2006), arXiv: physics/0605236
- [60] X. X. Liu, X. R. Lü, and Y. S. Zhu, *Chin. Phys. C* **39**, 103001 (2015), arXiv: 1505.01278[physics.data-an]